

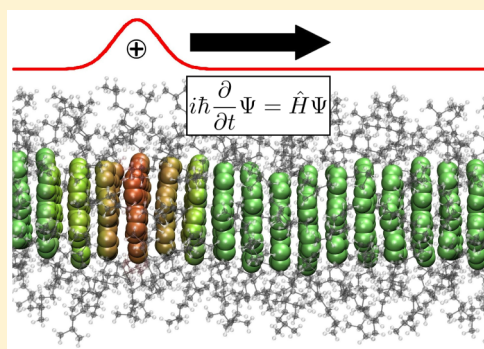
# Multi-Scale Approach to Non-Adiabatic Charge Transport in High-Mobility Organic Semiconductors

Alexander Heck,<sup>†,‡</sup> Julian J. Kranz,<sup>†</sup> Tomáš Kubař,<sup>†</sup> and Marcus Elstner<sup>\*,†,‡</sup>

<sup>†</sup>Department of Chemistry, Karlsruhe Institute of Technology, Kaiserstraße 12, 76131 Karlsruhe, Germany

<sup>‡</sup>Heidelberg Karlsruhe Research Partnership (HEiKA), Heidelberg University, Karlsruhe Institute of Technology (KIT), 76131 Karlsruhe, Germany

**ABSTRACT:** A linear scaling QM/MM model for studying charge transport in high-mobility molecular semiconductors is presented and applied to an anthracene single crystal and a hexabenzocoronene derivative in its liquid crystalline phase. The model includes both intra- and intermolecular electron–phonon couplings, long-range interactions with the environment, and corrections to the self-interaction error of density functional theory. By performing Ehrenfest simulations of the cationic system, hole mobilities are derived and compared to the experiment. A detailed picture of the charge carrier dynamics is given, and the performance of our method is discussed.



## 1. INTRODUCTION

Organic semiconductors (OSCs) are promising materials that are about to complement applications of traditional inorganic semiconductors. Achieving high mobility is of particular interest because this leads to better device performance like a higher efficiency of solar cells and faster switching speed of field effect transistors.<sup>1</sup> The OSCs showing the highest mobility are usually crystalline or semicrystalline molecules and polymers as well as liquid crystals.

One of the most important properties that influences charge transport is molecular packing because the relative orientation of the molecules has a large impact on their electronic coupling elements.<sup>2</sup> Additionally, the distortions of the equilibrium geometry due to local and nonlocal electron–phonon couplings play an essential role at finite temperatures.<sup>3</sup> The former introduces fluctuations of the site energies, whereas the latter mainly influences the electronic coupling between molecules, which in turn has a significant impact on the charge carrier dynamics.<sup>4–6</sup> Another factor that can largely influence the efficiency of OSC is the presence of impurities or structural defects in the material. They act as traps for the charge carrier, which reduces the mobility significantly and leads to activated transport.<sup>7,8</sup> In summary, this shows the pronounced importance of the atomistic structure and its dynamics for charge transport in organic semiconductors. However, a complete understanding of the charge dynamics in these materials is still missing yet urgently needed to improve device performance. The difficulty in the description of these materials lies in the fact that they are not as perfectly ordered as inorganic crystalline systems but also not completely disordered like amorphous systems. Conventional theories, however, are usually only applicable to the extreme cases of perfectly

ordered (inorganic) materials or completely disordered systems.<sup>7</sup>

In the most recent decade, different methodologies have successfully been applied for the description of charge transport in OSCs. On the one hand, there are several variants of hopping models.<sup>9</sup> In these models, the charge is restricted to a single molecule, and thermal activation can enable transitions to neighboring sites. Because of the localized description of the charge carrier, DFT calculations of large molecular systems with inclusion of environmental effects are affordable. These methods are usually applied to disordered systems like amorphous AlQ<sub>3</sub><sup>10</sup> or  $\alpha$ -NPD<sup>11</sup> but also to more ordered systems like liquid crystals,<sup>12–14</sup> polymers,<sup>15,16</sup> or partially disordered organic crystals.<sup>17–19</sup> On the other hand, model Hamiltonian approaches, parametrized from ab initio DFT calculations, have been further developed and successfully applied to ordered crystal structures, see, for example, refs 3 and 20 for recent reviews.

The limits of these models have been intensely discussed, i.e., lack of solutions for the full-bandwidth case in combination with nonlocal electron–phonon couplings.<sup>20</sup> The importance of nonlocal electron–phonon couplings has been emphasized several times; therefore, the restriction of theory to go beyond the small polaron model seems to be severe.<sup>21</sup> Because of the “nonexistence” of small polarons in high-mobility OSCs, the charge carrier is no longer localized, and a hopping description becomes inadequate.<sup>7,22,23</sup> Therefore, new methods have been proposed based on numerical propagation of the charge carrier.

**Received:** July 29, 2015

Applying a time-dependent Hamiltonian, the charge carrier can be propagated using stochastic, mean-field (MF; Ehrenfest) or surface hopping (SH) approaches.<sup>21,24,25</sup> MF and SH are semiclassical approaches, where the electronic wave function is propagated with the time-dependent Schrödinger equation, and the nuclear degrees of freedom follow classical trajectories. In principle, the nature of the charge carrier and the transfer mechanism is not predetermined in these approaches; therefore, they allow a localized as well as delocalized character of the charge carrier. However, because they are approximations to the full quantum propagation, they exhibit various drawbacks, as recently discussed in detail for the application to OSCs.<sup>24,25</sup> Nevertheless, valuable insights can already be obtained with model Hamiltonians, where the atomic resolution is discarded, and the nuclear vibration is reduced to few relevant modes.<sup>4,6,26</sup> Model Hamiltonians can give insight into basic principles, but detailed information about structure, dynamics, and their impact on the charge transport parameters have to be included for quantitative simulations of real materials. For instance, the electronic structure and electron–phonon interaction has to be resolved at an atomistic level. Such MF simulations have already been performed at various levels of quantum treatment, e.g., using a SSH Hamiltonian to describe fast transport through ordered systems like pentacene<sup>27</sup> using a DFT-based scheme for liquid crystals<sup>28</sup> or the intrachain transport in polymers applying an approximate DFT method DFTB.<sup>29</sup> Full atomic orbital DFT or DFTB approaches, however, exhibit a high computational demand; therefore, these simulations have to be restricted to small systems that are arguably representative of the bulk material.

In this work, we present a bottom-up simulation scheme free of tunable parameters, which allows for an unbiased simulation of charge transport in high-mobility organic semiconductors. This scheme should be able to predict the electronic properties of the material without input from the experiment. To this end, we will apply a computationally efficient linear scaling method for the propagation of the charge carrier, which is combined with a QM/MM scheme. This multiscale approach allows the simulation of thoroughly equilibrated extended molecular structures that are sufficiently large to be representative for the bulk material and that incorporate long-range disorder. We will describe the influence of the lattice fluctuations on the Hamiltonian as well as the impact of the propagating charge on the nuclear dynamics in a self-consistent way. Furthermore, the coupling to the classical environment will also be treated explicitly.

A similar method was already successfully applied to charge-transport in DNA<sup>30–32</sup> and proteins.<sup>33–35</sup> However, the different properties of biological systems and organic semiconductors made conceptual and technical changes of the methodology necessary. As is shown in the Appendix, the former description suffered from a self-interaction (SI) error that becomes apparent with delocalized charges and leads to erroneous charge carrier dynamics. In aqueous systems, like the previously studied DNA or proteins, the charge dynamics are dominated by the fluctuations of the polar environment, which obscures the impact of SI to some extent. Most organic semiconductors, on the other hand, are much less polar, which makes an SI-free description crucial. The SI also introduces errors to the electronic coupling elements between molecular sites, which will be corrected for in the current method. Further advancements in the current method are the consistent

calculation of local and nonlocal electron–phonon couplings, which play a crucial role in organic semiconductors. Although the former was previously captured by a precalculated correction term, the latter was still missing.

For an evaluation of our method, we will calculate hole mobilities for anthracene and a hexabenzocoronene derivative and compare them to experimental values. Furthermore, various aspects of our method are discussed, and a detailed picture of the charge dynamics is given.

## 2. METHODOLOGY

The goal is to derive an approximate simulation technique, which is efficient while still making use of essential atomistic information. For a consistent derivation, a total energy expression of the system is set up, which allows the use of well-known time-propagation schemes. However, a time-dependent QM description of a realistic system consisting of more than 1000 atoms is too costly, and several approximations are needed. The necessary approximations can be described as follows:

- First (section 2.1), we restrict the dynamic evolution of the electron density to certain parts of the electronic system, considering the remainder as electronically frozen. On the one hand, we divide the system into two regions, a quantum mechanical (QM) region where the charge carrier is located, and the remainder of the system, which is described by a classical force field (molecular mechanics: MM), i.e., we introduce the common QM/MM separation. However, we further simplify the description of the charge carrier by considering only several frontier orbitals around the Fermi level, e.g., highest occupied molecular orbitals (HOMOs) in the case of hole transfer and lowest unoccupied molecular orbitals (LUMOs) in the case of electron transfer, whereas strongly bound core states are approximated to stay unaffected in the charged system.<sup>32</sup> The wave function  $|\Psi\rangle$  describing the state of the charge carrier is then expressed as a linear combination of these orbitals. Therefore, we go beyond the standard QM/MM separation and do not only freeze states that are spatially, but also energetically, well-separated from the orbitals that are relevant for charge transport.

- Second (section 2.2), we partition the system via a fragment orbital (FO) formalism, which leads to a linear scaling with the system size. In molecular semiconductors, this partitioning refers naturally to the molecular building blocks. Therefore, the QM region is dissected into  $N$  QM regions (fragments) containing one organic molecule each. For every fragment, a quantum chemical calculation is performed, and the orbitals  $|\phi_m\rangle$  at each molecular fragment are used to build the wave function  $|\Psi\rangle$  of the charge carrier. As will be discussed below, several HOMO or LUMO orbitals per molecule can be included for the representation  $|\Psi\rangle$ .

- Third (section 2.3), we use an approximate DFT method for the QM calculations on the fragments, the density functional tight-binding (DFTB) method. This is a method derived from DFT that is roughly 2–3 orders of magnitude faster than DFT with medium-sized basis sets and thus accelerates the simulations significantly.

- Fourth (section 2.4), to derive coupled equations of motion for the electronic and nuclear subsystems, we apply the standard mean-field (Ehrenfest) propagation techniques. This allows a classical propagation of nuclei combined with a propagation of the time-dependent Schrödinger equation (or

time-dependent Kohn–Sham equation because it is derived from DFT) for the hole/electron wave function.

### 2.1. Total Energy Expression of the Charged System.

The starting point is the DFT energy of the charged system where environmental effects are included via classical force field terms.

$$E^+ = E_{\text{DFT}}[\rho] + E_{\text{MM}} + E_{\text{QM/MM}} \quad (1)$$

Here,  $\rho$  is the density of the QM zone including the hole charge carrier, and  $E_{\text{QM/MM}}$  is its electrostatic coupling to the neutral MM environment  $E_{\text{MM}}$ .

According to Janak's theorem,  $E_{\text{DFT}}[\rho]$  of a cationic system can be divided into the energy of the neutral QM zone with density  $\rho_0$  and the negative of its HOMO energy.

$$E^+ = E_{\text{DFT}}[\rho_0] - \langle \Psi | H[\rho_0] | \Psi \rangle + E_{\text{MM}} + E_{\text{QM/MM}} \quad (2)$$

Note that the calculation of a charged system with an odd electron number is also avoided in this way. For such cases, it is known that the SI error of DFT has tremendous influence on the localization of the charge.<sup>36</sup> In principle, there are three factors that may reduce the SI error: high relaxation energy, short distance between the fragments, and asymmetric fragment energies.<sup>36</sup> However, of these, we find the opposite case in organic semiconductors regarding all factors. Note that anionic systems would be treated analogously by adding the LUMO energy in eq 2. For clarity, we will restrict ourselves to the cationic case in this work.

Next,  $E_{\text{DFT}}[\rho_0]$  will also be approximated with the MM force field, which reduces the complexity dramatically and enables the energy of the neutral QM zone to combine with the environment

$$E_{\text{DFT}}[\rho_0] + E_{\text{MM}} + E_{\text{QM/MM}} \approx E_{\text{MM}}^{\text{tot}} + \Delta E_{\text{QM/MM}} \quad (3)$$

where  $E_{\text{MM}}^{\text{tot}}$  is the force field energy of the *whole* neutral system including all atoms of the MM as well as QM region, and  $\Delta E_{\text{QM/MM}}$  is the change of QM/MM interaction relative to the neutral system. Note that this approximation may even be superior to the original expression in eq 2 because it ensures that unoccupied molecules inside the QM region experience the same potential energy surface as the molecules of the classical environment. For example, the unit cell of molecular crystals might have a slightly different geometry when calculated with QM or MM methods. Therefore, treating equal molecules at different levels of theory, depending on their classification as QM or MM, could distort the translational symmetry of the crystal.

**2.2. Fragmentation of the System.** In the following, we make use of the morphology of organic semiconductors, which consist of weakly bound molecules. In contrast to Bloch waves of inorganic crystalline semiconductors, organic bulk materials preserve the underlying molecular electronic structure to a large extent (see Figure 1). This allows coarse-graining of the electronic structure of the complex by expanding the total density as a superposition of molecular densities and the hole wave function as a linear combination of molecular orbitals  $|\phi_m\rangle$  on fragment molecules A.

$$|\Psi\rangle \approx \sum_A \sum_{m \in A} a_m |\phi_m\rangle \quad (4)$$

$$\rho_0 \approx \sum_A \rho_A^0 \quad (5)$$

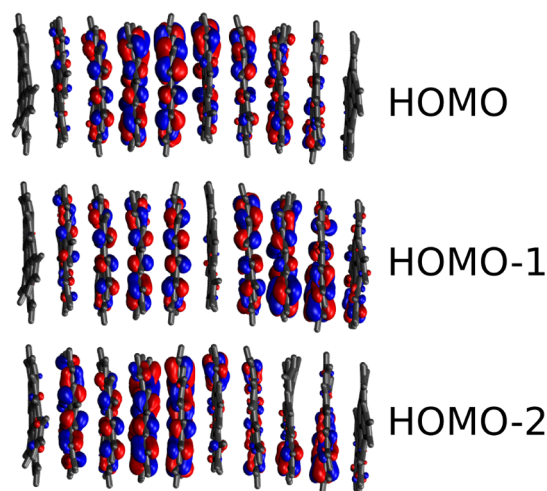


**Figure 1.** Highest molecular orbitals during a molecular dynamic simulation obtained at the PBE/def2-SVP level. The MOs of the complex are linear combinations of MOs of the individual molecules.

Inserting eqs 3 and 4 into 2, we obtain the total energy expressed in a fragment orbital basis

$$E^+ = E_{\text{MM}}^{\text{tot}} - \sum_{AB} \sum_{m \in A} \sum_{n \in B} a_m^* a_n \langle \phi_m | H[\rho_0] | \phi_n \rangle + \Delta E_{\text{QM/MM}} \quad (6)$$

Whenever needed, the representation in the atomic orbital basis is available via the expansion of FOs in AOs

$$|\phi_m\rangle = \sum_{\mu} c_{\mu}^m |\mu\rangle \quad (7)$$

leading to

$$E^+ = E_{\text{MM}}^{\text{tot}} - \sum_{\mu\nu} b_{\mu}^* b_{\nu} \langle \mu | H[\rho_0] | \nu \rangle + \Delta E_{\text{QM/MM}} \quad (8)$$

with  $b_{\mu} = \sum_A \sum_{m \in A} a_m c_{\mu}^m$ . However, the FO description gives access to corrections of the QM method and leads to better performance, as will be shown in section 2.5.

In most cases, the hole wave function of the system  $|\Psi\rangle$  is described well by a linear combination of HOMOs on each fragment. Additional FOs can be included in cases where lower lying orbitals have similar energy. The construction of coarse-grained FO basis functions shows some analogies to contracted basis sets like GTOs. Whereas several Gaussians are contracted to yield a suitable atomic basis function, in our case, several AOs are contracted into an FO basis function that can properly describe a hole on this fragment. The dimension of the Hamilton matrix in this coarse-grained representation is significantly reduced compared to a full AO basis; however, it is still able to describe the hole wave function accurately. Although FOs on the same fragment are orthogonal by construction, there is a small overlap between FOs on different fragments. To facilitate further calculations, we orthogonalize the included FOs at every step with the Löwdin method.<sup>37</sup> In this work, fragment orbitals  $|\phi_m\rangle$  and their FO coefficients  $c_{\mu}^m$  will denote the respective quantities after the orthogonalization procedure, whereas a prime will be added to denote their nonorthogonalized counterparts.

**2.3. Approximations in the Quantum Calculations.** In a next step, the matrix elements  $\langle \mu | H | \nu \rangle$  in eq 8 have to be computed with a quantum chemical method, which can be HF,



DFT, or a semiempirical one. For simulations over several ps and meaningful statistical sampling, DFT calculations are prohibitively slow, and greater efficiency is needed. Recent tests have shown that semiempirical methods are able to compute these matrix elements with very good accuracy, comparable to HF and DFT.<sup>38–41</sup> For this reason, we use the approximate DFT method DFTB, which provides an additional acceleration of 3 orders of magnitude compared to DFT-GGA functionals.<sup>42,43</sup> DFTB relies on a Taylor expansion of the total energy around a reference density. There exist several levels of DFTB depending on the order of the expansion. DFTB1,<sup>44,45</sup> DFTB2,<sup>46</sup> and DFTB3<sup>47</sup> denote a first-, second-, and third-order expansion, respectively. By equating  $\langle \mu | H[\rho_0] | \nu \rangle = H_{\mu\nu}^{\text{DFTB}}$ , we obtain, for example, within the DFTB2 formalism

$$H_{\mu\nu}^{\text{DFTB}} = H_{\mu\nu}^0 + S_{\mu\nu} \sum_c \Delta q_c \left[ \frac{1}{2} (\gamma_{ac} + \gamma_{bc}) \right] \quad \forall a, b, \mu \in a, \nu \in b \quad (9)$$

$H_{\mu\nu}^0$  are DFTB1 Hamilton matrix elements, where the neutral atomic density is used in the effective Kohn–Sham potential, allowing the tabulation of these integrals. The  $\gamma$  functions are introduced in DFTB2 and describe how deviations from the reference density (expressed as Mulliken charge differences  $\Delta q_c$  on atom  $c$ ) affect the total energy. The charge-dependent terms require a self-consistent solution, which is beneficial for polar systems with a sizable charge transfer between the atoms. For nonpolar molecules like the organic molecules of interest here, the charge-density fluctuations are negligible, i.e., the DFTB1 approach gives nearly identical results to DFTB2 and DFTB3.<sup>48</sup> At the same time, the self-consistent solution due to the charge dependence in DFTB2 and DFTB3 requires five to ten times more computation time than the non-self-consistent DFTB1 scheme. Therefore, we limit our calculations to DFTB1 due to the nonpolar character of the investigated molecules, gaining an additional order of magnitude in speed.

For long-range interactions, the density is represented in DFTB as atomic point charges, which leads to the following QM/MM term

$$\Delta E_{\text{QM/MM}} = \sum_A \sum_{m \in A} |a_m|^2 \sum_K \sum_{\alpha \in A} \left( \frac{\Delta q_{\alpha}^m q_K^0}{|R_{\alpha} - R_K|} \right) \quad (10)$$

where  $q_K^0$  is the force-field partial charge on atom  $K$  of the neutral environment, and  $\Delta q_{\alpha}^m = \frac{1}{2} \sum_{\mu} \sum_{\nu \in \alpha} (c_{\mu}^* c_{\nu}^{\mu} S_{\mu\nu} + c_{\nu}^* c_{\mu}^{\nu} S_{\nu\mu})$  is the change of Mulliken charge on atom  $\alpha$  resulting from a hole residing in orbital  $m$ .

By applying the variational principle, we obtain an additional term in our Hamiltonian

$$H_{\mu\nu}^{\text{QM/MM}} = \frac{1}{2} S_{\mu\nu}^{\alpha\beta} \sum_K q_K^0 \left( \frac{1}{R_{\alpha K}} + \frac{1}{R_{\beta K}} \right) \quad (11)$$

where  $\mu$  is located on atom  $\alpha$ ,  $\nu$  is on atom  $\beta$ , and  $R_{\alpha K}$  is short for  $|R_{\alpha} - R_K|$ .

**2.4. Simultaneous Propagation of Electronic and Nuclear Degrees of Freedom.** With the total energy expression in hand, equations of motions for atoms and electrons can be derived in the framework of time-dependent DFT. Similarly to previous work,<sup>30,32</sup> we apply the Lagrangian formalism

$$L = T - V \quad (12)$$

$$T = \sum_K \frac{1}{2} M_K \dot{R}_K^2 + \langle \Psi | -i \frac{\partial}{\partial t} | \Psi \rangle \quad (13)$$

$$V = E_{\text{MM}}^{\text{tot}} - \langle \Psi | H[\rho_0] | \Psi \rangle + \Delta E^{\text{QM/MM}} \quad (14)$$

The evaluation of the Lagrangian equations is detailed in the [Appendix](#) and leads to the following equation of motion for the electrons

$$\dot{a}_m = -i \sum_n a_n H_{mn} - \sum_n a_n \langle \phi_m | \dot{\phi}_n \rangle \quad (15)$$

where  $H_{mn}$  are the matrix elements of the FO Hamiltonian from [eq 19](#) incorporating QM/MM interactions. The last term in [eq 15](#) vanishes if a spatially fixed orthogonal basis (e.g., plane waves) is used. In an atom-centered basis set, however, additional terms arise from the time-dependent origin of the basis functions.<sup>49</sup> By writing  $\langle \phi_m | \dot{\phi}_n \rangle$  as  $\langle \phi_m | \frac{\partial}{\partial R} | \phi_n \rangle \frac{\partial R}{\partial t}$ , it becomes clear that the coupling becomes important for high-velocity collisions and atoms that are close to each other, but it vanishes for sites that are far apart and at low temperature. As first approximations, these terms are therefore omitted in the propagation.

However, the coupling terms  $\langle \phi_m | \dot{\phi}_n \rangle$  also give rise to transitions between orbitals on the same molecule, whose impact we will examine in the following. In general, if the nonadiabatic coupling between  $|\phi_m\rangle$  and  $|\phi_n\rangle$  is small while they are energetically crossing, the charge carrier will follow its initial state through the crossing region and end up in the excited state. If, on the other hand, the coupling is large, the charge carrier will stay in the ground state all the time. To evaluate the influence of the nonadiabatic coupling between the degenerate FOs, we apply two different approaches in the simulation of HBC. (1) We take no special care in the expansion of the charge carrier wave function when the (nearly) degenerate FO basis functions of one molecule cross. A charge carrier residing in the highest FO will therefore remain in the highest FO after a crossing event, which corresponds to the limit of a large nonadiabatic coupling. (2) After the propagation  $t_1 \rightarrow t_2$  is performed in the basis at  $t_1$ , we project the obtained wave function  $|\Psi(t_2)\rangle_{t_1}$  onto the new basis at  $t_2$ .

$$|\Psi(t_2)\rangle_{t_2} = \sum_m |\phi_m(t_2)\rangle \langle \phi_m(t_2) | \Psi(t_2) \rangle_{t_1} = \sum_{mn} a_n |\phi_m(t_2)\rangle \langle \phi_m(t_2) | \phi_n(t_1) \rangle \quad (16)$$

This way, the charge carrier is forced by projection to the orbital with the same character, which corresponds to the limit of zero nonadiabatic coupling. We approximate  $\langle \phi_m(t_2) | \phi_n(t_1) \rangle$  by calculating  $\langle \phi'_m(t_2) | \phi'_n(t_1) \rangle$  on each site in the non-orthogonal basis.<sup>50</sup> Note that a projection would only be norm-conserving with a complete basis set. Therefore, the wave function has to be renormalized after the projection.

Within the Lagrangian formalism, we obtain for the nuclear degrees of freedom

$$M_K \ddot{R}_K = -\frac{\partial E_{\text{MM}}^{\text{tot}}}{\partial R_K} + \frac{\partial}{\partial R_K} \left( \sum_{mn} a_m^* a_n \langle \phi_m | H | \phi_n \rangle \right) - \frac{\partial}{\partial R_K} \Delta E^{\text{QM/MM}} \quad (17)$$

where  $k$  denotes  $x, y, z$  of atom  $K$ . The first term originates from the force-field and would be the only contribution in a standard molecular dynamic simulation (MD) of a neutral system. The sum in parentheses contains the diagonal and off-diagonal elements of the coarse-grained Hamiltonian. The derivatives of diagonal elements with respect to atomic coordinates are related to the internal relaxation of a single fragment, whereas the derivatives of intermolecular electronic couplings yield the forces resulting from bonding and antibonding linear combinations of FOs; terms that are missing in a localized hopping description of the charge dynamics. The last term covers the interaction of the charge carrier with the MM environment and is related to the external (outer-sphere) reorganization energy.

After transformation of the FO Hamiltonian into the AO basis, we arrive at the following expression for the force within the applied DFTB1 formalism

$$M_k \ddot{R}_k = -\frac{\partial E_{\text{MM}}^{\text{tot}}(q_A^0, \Delta q_A)}{\partial R_k} + \sum_{mn} \sum_{\mu\nu} a_m^* a_n c_{\mu}^m c_{\nu}^n \left( \frac{\partial H_{\mu\nu}^0}{\partial R_k} - \delta_{mn} \epsilon_m \frac{\partial S_{\mu\nu}}{\partial R_k} \right) \quad (18)$$

where  $E_{\text{MM}}^{\text{tot}}(q_A^0, \Delta q_A)$  denotes the force field energy of the total system with adapted partial charges; the derivation is shown in the [Appendix](#).

**2.5. Advantages of the DFTB-Based Fragment Orbital Approach.** In the development of quantum chemical approaches, one strives to balance the computational speed and accuracy required for the specific application. Here, we have chosen a fragment orbital approach in combination with a QM/MM algorithm. This has a computational advantage but also one connected with accuracy.

First, the fragmentation allows for an independent calculation of the molecular subsystems. This leads to a linear-scaling ( $O(N)$ ) computational scheme, where the computer time increases linearly with system size. Furthermore, there is no threshold in system size for the efficiency gain, because no larger systems than the monomers have to be considered, in contrast to other  $O(N)$  schemes, where dimers/trimers or larger buffer regions have to be computed, depending on the particular implementation. This is obviously due to the combination with a force field and the particular constitution of the systems treated here, where no covalent bonds are dissected upon fragmentation of the system.

Equally important is the aspect of accuracy, which is enhanced, perhaps surprisingly, by this approximation. There are two problems to be considered when using an approximate method like DFT and HF approaches employing small (minimal) basis sets. One is connected to the basis set issue, and the other is related to the inherent limitations of mean field electronic structure calculations. Yang et al. illustrated the problems related to the fractional charge effect in DFT and HF, which are critical for the description of charge transfer.<sup>51,52</sup> In approximate DFT functionals, the SI is not canceled by the exchange term as it is in HF; therefore, the electrons exhibit a spurious repulsion, which leads to the overdelocalization of electrons, in particular for half-occupied frontier orbitals. This leads to an artificial spread of the charge distribution, as we demonstrated for the case of DNA.<sup>32</sup> By contrast, HF overlocalizes; therefore, it is also not reliable to predict the size and spread of the charge carrier. On the other hand, this DFT problem leads to drastic errors in the Kohn–Sham energies, i.e., the HOMO and LUMO energies deviate from the

IP or EA by several eV. This is obviously a huge problem for any propagation scheme (like Ehrenfest) because the site energies determine the energy landscape, which can be significantly distorted when different sites have different errors (whereas a constant error would be no problem). Therefore, one would expect any approximate DFT to exhibit significant errors for the energy landscape of heterogeneous systems with fragments of different chemical constitution like, e.g., interfaces. Therefore, Ehrenfest simulations using approximate DFT<sup>29,53</sup> (approximate functional, small basis sets) should be interpreted with some caution. This has also recently been discussed for organic electronic applications.<sup>54</sup> Long-range corrected functionals present a merely partial cure because they have to be system-specifically tuned and are not size-consistent.

Bearing this in mind, the FO approach, besides the intuitive description of charge transport through molecular systems within a basis of charge carrying molecules, also has several technical advantages:

(1) Basis set effects: in DFTB, atomic orbitals are computed from atomic DFT calculations and are then used to evaluate the Hamilton  $H_{\mu\nu}^0$  and overlap  $S_{\mu\nu}$  matrix elements. Slightly confined versions of the free atomic orbitals are used to achieve an optimal description of the electronic density in the bonding region.<sup>44,45</sup> Because of this procedure, however, the charge transfer (CT) integrals between distant fragments  $\langle \phi_m | H[\rho_0] | \phi_n \rangle$  (eq 6) are severely underestimated.<sup>40</sup> Thus, it is difficult to achieve an adequate description over a long-range of inter-atomic distances with a minimal basis set. Therefore, we have suggested to capture some benefits of a double- $\zeta$  basis using the FO approach without actually increasing the computational effort.

We use the confined basis for the description of intra-molecular interactions to obtain the correct energy and nodal structure of the FOs. The downside of the confinement, i.e., the underestimation of intermolecular interactions, is mitigated by lifting the confinement for the calculations of intermolecular matrix elements. To this end, the FO coefficients  $c_{\mu}^m$  are obtained first in parallel calculations of the independent molecules in their electrostatic environment, applying the confined standard parameter set.<sup>46</sup> In a second step, the Hamiltonian of the complex in the (non-orthogonal) FO basis is constructed as

$$\mathbf{H}_{\text{FO}} = \mathbf{C}^T \mathbf{H}_{\text{AO}} \mathbf{C} = \mathbf{C}^T [\mathbf{H}^{\text{DFTB}} + \mathbf{H}^{\text{QM/MM}}] \mathbf{C} \quad (19)$$

where  $\mathbf{C}$  is a block-diagonal matrix of the fragment orbital coefficients  $c_{\mu}^m$ , and  $\mathbf{H}^{\text{DFTB}}$  and  $\mathbf{H}^{\text{QM/MM}}$  are the matrices of the Hamilton elements of eqs 9 and 11, respectively.  $\mathbf{H}_{\text{AO}}$  is a block matrix, where standard parameters are employed for the diagonal blocks, and a less confined set is used for the off-diagonal blocks, which was shown to yield intermolecular couplings in an excellent agreement with FO DFT calculations.<sup>38,39</sup> The FO overlap matrix, which is needed for the subsequent orthogonalization of the FO basis, is obtained analogously.

(2) The FO scheme also allows an efficient correction of our method for the SI error of DFT. This has 2 parts:

(a) The total energy in eq 2 has the QM contribution, which consists of  $\langle \Psi | H[\rho_0] | \Psi \rangle$ . This term is a simple tight-binding Hamiltonian, which depends only linearly on the electron density. This implies that this energy contribution exhibits the desired “straight-line” behavior when computing the charge-dependent energies,<sup>52</sup> i.e., it is SI-free. This has also been discussed in detail for DFTB,<sup>55</sup> and an analysis of the influence

of SI on the charge carrier dynamics is shown in the Appendix. SI occurs in such density expansion schemes, as presented in ref 32, for example, as second order energy terms, which depends on the square of the charge density. Therefore, the total energy expression in eq 2 is SI-free, and we do not expect an artificial delocalization of charge over the fragments. SI in an uncorrected scheme would occur as overdelocalization of the charge carrier over the different sites.

(b) However, the SI error is also present in the calculations of the CT parameters, i.e., the FO matrix elements. On the one hand, HOMO and LUMO orbital energies  $\epsilon_m = H_{mm}$  show large deviations from the respective IP and EA values that are not systematic, i.e., a different error occurs for different chemical species. This does not pose a problem for the homogeneous materials studied here, but when CT over different chemical moieties is studied, the site energies can be corrected using an FO approach, which is not possible in AO methods. Such a correction scheme has been discussed in detail in ref 56. The relative site energies have to be calculated only once at a high-level of theory to obtain the correct reference value, and then the erroneous site energies can be corrected during the Ehrenfest simulation by applying a constant shift. On the other hand, the SI leads to a systematic underestimation of intermolecular electronic couplings  $H_{mn}$  ( $m \neq n$ ).<sup>57</sup> The reason behind this is the exponentially decaying exchange-correlation potential, whereas the correct potential had to decay with  $1/r$  in order to cancel the SI. As a result, local exchange-correlation functionals yield too small contributions to the coupling at intermolecular distances. By varying the amount of exact HF exchange from 0 to 100%, the electronic coupling increases by roughly a factor of 2.<sup>57</sup> The same underestimation can be expected using DFTB because during its parametrization electronic couplings are obtained with the PBE functional. It has been shown that the deviation is systematic and that the intermolecular DFTB coupling can be corrected with a universal scaling factor of 1.540 for holes<sup>38</sup> and 1.795 for electrons.<sup>39</sup> The same correction factors are applied here to the intermolecular coupling elements.

Therefore, the FO scheme not only accelerates the computations significantly, it allows also the accuracy to be improved in a simple way by correcting (i) for basis set effects, (ii) for SI at the FO total energy level, and (iii) constructing a very accurate FO Hamiltonian  $H_{mn}$ , where the site energies  $\epsilon_m = H_{mm}$  are corrected to reproduce IP/AE differences (similar idea as in long-range corrected DFTB<sup>54</sup>), and the electronic couplings  $H_{mn}$  ( $m \neq n$ ) are corrected by scaling.<sup>38,39</sup>

### 3. EVALUATION AND APPLICATION

Ultrapure single crystals are prototypical systems for the understanding of intrinsic charge transport phenomena because defects and impurities would obscure the material-specific (intrinsic) mobility by providing trap states.<sup>8</sup> Therefore, we will simulate the charge carrier dynamics in an anthracene single crystal, which can be obtained at very high purity for the experiment,<sup>58</sup> and calculate the anisotropic mobility along different crystallographic axes (see Figure 2). The other system for testing will be a liquid crystal of hexabenzocoronene (HBC) with racemic branched (3,7-dimethyloctanyl) side chains.<sup>59</sup> This molecule features an interesting electronic structure with degenerate frontier orbitals and gives rise to more disordered morphologies.

The anthracene single crystal was modeled as a supercell consisting of  $20 \times 20 \times 20$  unit cells. The initial coordinates

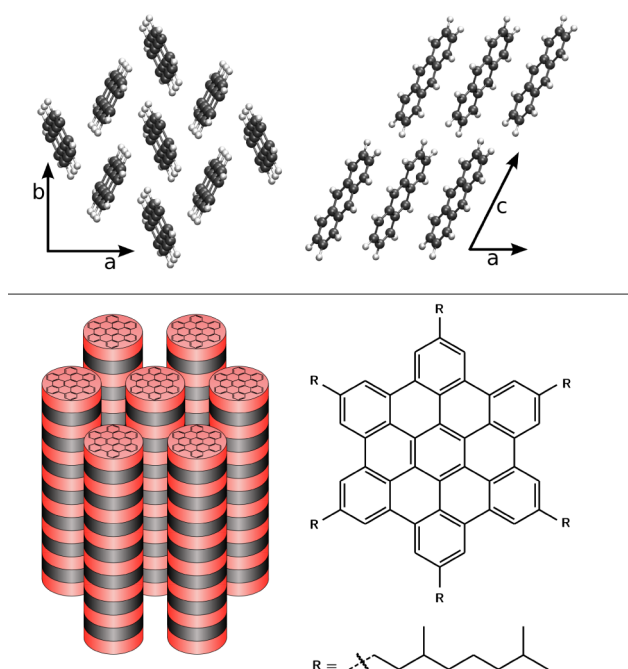


**Figure 2.** Crystal structure of anthracene (top) and hexagonal liquid crystalline phase of HBC (bottom), where monomers (black/red) stack with a mutual twist of  $30^\circ$  around the columnar axis.

were obtained from the crystal structure.<sup>60</sup> The HBC liquid crystal was modeled as 9 columns arranged in a hexagonal lattice, each consisting of 110 molecules. The molecules were stacked with a twist of  $30^\circ$ , and a random configuration of the stereogenic centers at the side chains was used. The GAFF<sup>61</sup> force field parameters were used for bonded and VdW interactions, whereas the partial charges were fitted individually. RESP<sup>62</sup> fitted charges were used for anthracene, and CM3<sup>63</sup> corrected partial charges were used for HBC. Periodic boundary conditions with particle-mesh Ewald electrostatics were used in all simulations. Anthracene was simulated at 300 K, and HBC was simulated in its liquid crystalline phase at 400 K. Temperature and pressure equilibrations of the neutral systems lasted for several nanoseconds in both cases. During the production runs, the Parrinello–Rahman barostat and the Nosé–Hoover thermostat were used to yield a correct canonical ensemble at 1 bar and the respective temperature.

The presented method is implemented in a local version of Gromacs 4.6,<sup>64</sup> which was also used for the equilibration runs. Apart from the presented methodology, DFTB calculations were performed with DFTB+ 1.2,<sup>65</sup> whereas other QM calculations were performed with ADF 2012<sup>66</sup> and Turbomole 6.5.<sup>67</sup>

**3.1. Evaluation of Site Energies.** The diagonal elements of the coarse-grained Hamiltonian represent the energy of the system with one electron taken out of the HOMO of the respective molecule. This value would be exactly the vertical IP of that molecule in SI-free DFT. In most practical calculations, however, the orbital energies are not corrected for the SI, which is the reason why the HOMO energy is merely an approximation of the IP. To assess if the difference between IP and HOMO energy will have any effect on our calculations, we compare their time evolution during an MD simulation of an anthracene crystal. The IP is calculated as the difference of the self-consistent DFTB2 total energies of the cationic and neutral molecule and compared to the (non)self-consistent



HOMO energy at the (DFTB1) DFTB2 level. As can be seen in Figure 3, there is a large difference between site energies

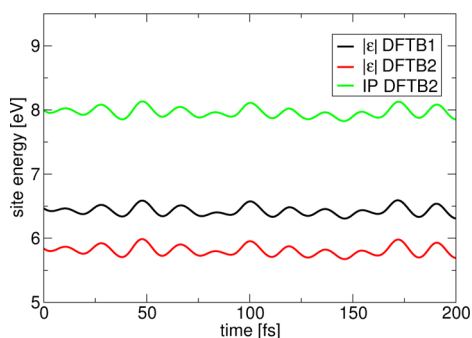


**Figure 3.** Comparison of HOMO energies obtained without (black) and with self-consistency (red) to the ionization potential (green) along an MD simulation of an anthracene crystal. Site energies are shifted but show the same fluctuations.

obtained with the different approaches. However, the difference constitutes a constant shift and has therefore no effect on the physics of the system. The energy fluctuations, on the other hand, are the same with all approaches. Note that in systems containing multiple types of molecules, like organic polymer blends or doped materials, special care has to be taken to correctly reproduce the relative energies. Approximating site energies with HOMO energies might lead to erroneous energetics in these cases. In a previous work, we presented a detailed comparison between DFT and DFTB2 site energies and their fluctuations along MD trajectories.<sup>40</sup>

**3.2. Evaluation of Electronic Couplings.** The electronic couplings obtained with DFTB were recently benchmarked against high-level ab initio calculations for hole<sup>38</sup> and electron<sup>39</sup> transfer. Here, we further assess if the excellent performance of DFTB is also transferable to the herringbone crystal structure of anthracene by comparing the electronic coupling between nearest neighbors to DFT calculations. As can be seen in Table 1, remarkably good agreement with DFT calculations at the

**Table 1. Electronic Coupling between Nearest Neighbors for the Anthracene Crystal Structure Obtained with our DFTB Method and with DFT at the B3LYP/TZ2P Level**

direction to nearest neighbor	electronic coupling [meV]	
	DFT	DFTB
same unit cell	20.8	25.5
<i>b</i> -axis	47.9	41.0
<i>c</i> -axis	0.8	0.0

B3LYP/TZ2P level is achieved. The highest electronic coupling is found along the *b*-direction with 48 meV. The coupling between the two molecules in the unit cell is, with 21 meV, approximately a factor of 2 smaller, and the coupling along the *c*-direction is nearly zero. Note that structural fluctuations during the MD simulation will also give rise to nonzero electronic couplings along the *c*-direction.

**3.3. Influence of the Environment.** To evaluate the influence of the environment, we calculated the site energies of a single HBC molecule at every step along a 100 ps MD simulation including and excluding the electrostatic potential (ESP) of the environment. The standard deviation of the site energies increases from 61 to 81 meV due to the electrostatic

interactions with the environment. The time scale of those fluctuations was examined with a power spectrum (Fourier transform of the autocorrelation function).

As can be seen in Figure 4, the site energies are mainly modulated by an intramolecular vibration with  $\tilde{\nu} = 1720 \text{ cm}^{-1}$ .

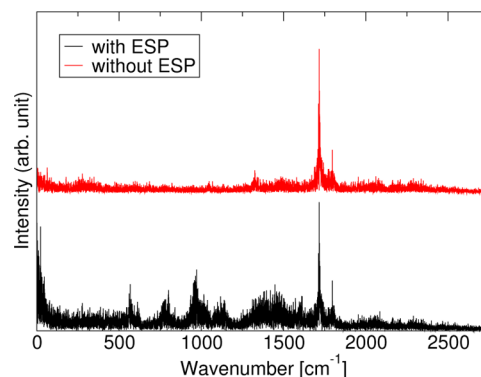


**Figure 4.** Power spectrum of site energies with and without the electrostatic potential (ESP) of the environment. Intramolecular vibrations give rise to a distinct peak at  $\tilde{\nu} = 1720 \text{ cm}^{-1}$ , whereas a broad distribution of slow oscillations are introduced by the environment.

The environment, on the other hand, gives rise to several site fluctuations with lower frequencies with dominant contribution below  $100 \text{ cm}^{-1}$ .

**3.4. Electron–Phonon Coupling.** An important aspect of our method is the inclusion of electron–phonon coupling. We tested how the molecular relaxation affects the site energies of anthracene and HBC. The energy (eq 6) of a single molecule *A* was minimized in the neutral ( $|a_m|^2 = 0 \forall m \in A$ ) and cationic ( $|a_m|^2 = \delta_{m,\text{HOMO}}$ ) state. As expected, the relaxation of the structure is accompanied by a decrease of the site energy  $|H_{mm}|$ , thus effectively lowering the IP. As can be seen in Figure 5, the

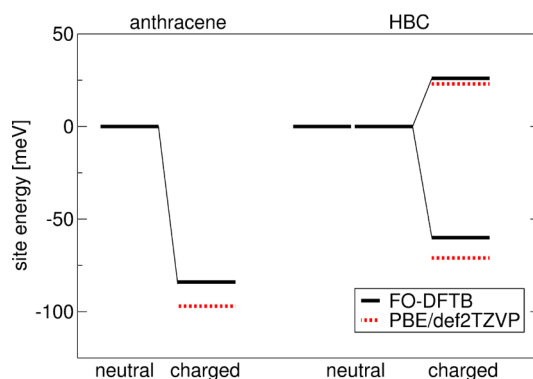


**Figure 5.** Relaxation of site energies upon charging. Data for anthracene and HBC molecules obtained with the presented multiscale approach as well as DFT calculations at the PBE/def2-TZVP level.

HOMO of anthracene gets shifted by 84 meV. For HBC, Jahn–Teller distortion can be observed, causing the degenerate site energies to split by 86 meV. The relaxation of 60 meV with respect to the neutral HOMO level corresponds to  $\sim 3/4$  of the anthracene value. This is in accordance with the finding that larger aromatic cores exhibit smaller internal reorganization energies.<sup>68</sup> These values are slightly smaller than DFT results at the PBE/def2-TZVP level, where a shift of 97 meV is found for

anthracene, and the splitting and relaxation in HBC are 94 and 71 meV, respectively.

**3.5. Picture of the Charge Transport.** Each charge dynamics simulation was preceded by a 500 fs simulation where the charge was restricted to a single molecule to allow for a relaxation caused by the charge carrier. In the subsequent charge dynamics simulations, the lowest eigenvector of the coarse-grained Hamiltonian was used as the starting wave function. The time step of the MD was 1 fs; note that the Runge–Kutta method used to integrate the time-dependent Schrödinger equation performs a large number of shorter time steps internally. The QM zone of the anthracene systems consisted of 18 sequential molecules in the direction of the respective crystallographic axis. For HBC, the QM zone consisted of 30 molecules along one columnar stack, and a capping scheme was applied to substitute the side chains. Every single simulation of the propagation of a charge carrier evolves differently due to different initial conditions, and averaging over an ensemble of simulations is needed to derive observable quantities. Nevertheless, all these individual simulations share some common features, which will be discussed on two selected trajectories.

First, we take a look at a simulation of anthracene. As can be seen in Figure 6 (left), the charge initially forms a polaron that

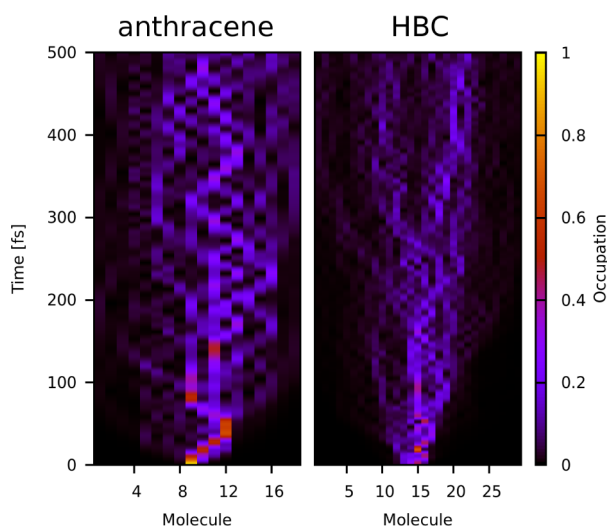


**Figure 6.** Exemplary time evolution of the hole in anthracene and HBC. The initially localized polaron in anthracene is scatted at  $\sim 50$  fs and dissociates until it is completely delocalized at the end of the simulation. For HBC, the polaron dissociates after 300 fs to two separate wavepackets.

travels over several sites. After  $\sim 50$  fs, the charge is scattered on a phonon, and the polaron dissociates. Following this event, the localized wave function is continuously broadened, and it is delocalized over nearly the entire system after less than 500 fs. Notably, the charge carrier is transferred very fast between neighboring molecules without significant residence time. The occupation of one site lasts only a few tens of femtoseconds. Such an activation-less transfer is expected considering the relatively high electronic coupling and small reorganization energy of anthracene, and it underlines the impact of nuclear vibrations on the dynamic evolution of the charge carrier.

A similar behavior is found for HBC (Figure 6 right) with a progressive broadening of the charge carrier wave function. Additionally, a splitting of the wavepacket can be seen,

especially after 300 fs, two diverging wavepackets can be observed. Such a behavior is a result of the Ehrenfest approach, where the system evolves on an ensemble of adiabatic states. In contrast to surface hopping simulations, it is not possible to obtain relaxation to a single adiabatic surface, either where the charge is represented by the left wavepacket or the right wavepacket. Similar observations were made with a very similar approach in DNA.<sup>30</sup> Application of a mean field approach led to partial delocalization in poly adenine stacks, whereas restricting the nuclear dynamic to a single adiabatic surface by applying a surface hopping approach led to localized charge. However, application of a surface-hopping description to our systems is quite involved due to frequent crossings of adiabatic surfaces resulting from the relatively small electronic coupling and energetic disorder of the molecular sites.

**3.6. Charge Carrier Mobilities.** Next, we calculate hole mobilities and compare them to experimental values. The mobility  $\mu$  is derived from the diffusive motion of the charge carrier according to the Einstein–Smoluchowski equation

$$\mu = \frac{eD}{k_B T} \quad (20)$$

where  $k_B$  is the Boltzmann constant,  $e$  denotes the elementary charge, and the diffusion constant  $D$  is obtained as

$$D = \frac{\langle \Delta x^2(t) \rangle}{nt} \quad (21)$$

where  $\langle \Delta x^2(t) \rangle$  is the mean squared displacement of the charge at time  $t$ , and  $n$  takes the value of 2, 4, or 6 for 1-, 2-, or 3-dimensional systems, respectively. The mean squared displacement is defined as

$$\langle \Delta x^2(t) \rangle = \sum_A (x_A(t) - x_0)^2 p_A(t) \quad (22)$$

where  $x_A(t)$  denotes the center of mass of molecule  $A$ , and  $x_0$  is the initial position of charge carrier at  $t = 0$ .  $p_A(t)$  is the occupation of molecule  $A$  at time  $t$  given as  $p_A(t) = \sum_{m \in A} |a_m|^2$ . To capture the influence of different starting conditions, we averaged the mean square displacement over 100 simulations. The mobility was obtained from a linear fit of  $\langle \Delta x^2(t) \rangle$  over time during the first 100 fs.

As can be seen from Table 2, an excellent agreement with time-of-flight (TOF) experiments is achieved for anthracene. The crystallographic  $b$  direction has been correctly identified as

**Table 2.** Hole Mobilities for Anthracene at 300 K along Crystallographic Axes as well as for Liquid Crystalline HBC at 400 K along the Columnar Stacking Direction, and HBC(1) and HBC(2) Denote the Different Approaches to Intramolecular Orbital Transitions (see section 2.4)<sup>a</sup>

system	mobility [ $\text{cm}^2/(\text{V s})$ ]		ref
	calculated	experimental	
anthracene (a)	0.80	1.14 (TOF)	58
anthracene (b)	1.94	2.93 (TOF)	58
anthracene (c)	0.48	1.05 <sup>a</sup> (TOF)	58
HBC(1)	1.16	$\sim 0.4$ (PR-TRMC)	69
HBC(2)	1.55	$\sim 0.4$ (PR-TRMC)	69

<sup>a</sup>An orthogonalized coordinate system  $a \perp b \perp c'$  was used in the experiment, where  $c'$  differs by  $\sim 35^\circ$  from the crystallographic  $c$ -direction used in our simulations.



the best transport direction with a mobility of  $1.94 \text{ cm}^2 \text{ V}^{-1} \text{ s}^{-1}$ . The transport along the *a*- and *c*-directions is similarly fast but slower than along the *b*-direction. The calculated mobilities are within a factor of 2 of the experimental values.

The calculated mobilities for HBC deviate slightly more from the experimental values obtained with the pulse-radiolysis time-resolved microwave conductivity technique (PR-TRMC) but are still within the same order of magnitude. The different treatment of transitions between degenerate orbitals on one site leads to a notable difference in the calculated mobilities; however, both values are still reasonable compared to experimental values. Without nonadiabatic coupling between the degenerate HOMOs (method 2), the charge can pass the crossing events of the HOMOs and continue in the excited state. This excitation counteracts the energetic relaxation due to polaron formation and aids in achieving resonance with nonrelaxed (unoccupied) neighboring sites. Therefore, a higher mobility can be observed within this approach. The mobility is overestimated in HBC in contrast to anthracene. However, these values can be seen as an upper boundary because impurities, defects, and losses at the contacts are not taken into account in our simulations. A further explanation for the underestimated mobility in anthracene in contrast to the overestimation in HBC is that our anthracene simulations are artificially restricted to one dimension, whereas the charge carrier can circumvent mobility bottlenecks introduced by thermal vibrations in an actual 3-dimensional system. Note that the charge transport through HBC, on the other hand, is truly 1-dimensional.

**3.7. Charge Transport Mechanism.** The time evolution of the wave function following Ehrenfest dynamics shows a spreading similar to that of a 1-dimensional wavepacket propagated with the Schrödinger equation known from quantum mechanics text books. The spreading is an ensemble property and therefore does not directly inform about the localization/delocalization of the charge carrier. A measure of intrinsic delocalization can be obtained from the delocalization of the adiabatic states.

$$|\varphi_i\rangle = \sum_m c_m^i |\phi_m\rangle \quad (23)$$

Therefore, we calculated the adiabatic states for HBC and the anthracene *b*-direction along the 100 simulations by diagonalizing the fragment orbital Hamiltonian at every step. The number of molecules over which one adiabatic state *i* is delocalized was defined as  $N_{\text{del}}^i = \frac{1}{\sum_A (p_A^i)^2}$ , where  $p_A^i$  is the

charge on molecule *A* in state *i* given as  $p_A^i = \sum_{m \in A} |c_m^i|^2$ . The delocalization fluctuates strongly, and the wave function was occasionally delocalized over up to 20 HBC molecules or 10 anthracene molecules. However, these are quite rare events, and the delocalization is significantly smaller in average. The averaged delocalization for a certain energy interval as well as the density of states (DOS) are shown in Figure 7. As can be seen from the figures, the DOS can be described very well by a Gaussian distribution with a standard deviation of 0.11 and 0.12 eV for HBC and anthracene, respectively. The states at the tails of the DOS are significantly stronger localized compared to the states near the center. However, even the localized states at the tails are still not restricted to a single molecule. Note that for anthracene, in contrast to HBC, the DOS and delocalization do not represent bulk material properties because we are restricting our simulations to 1-dimensional QM zones. Rather

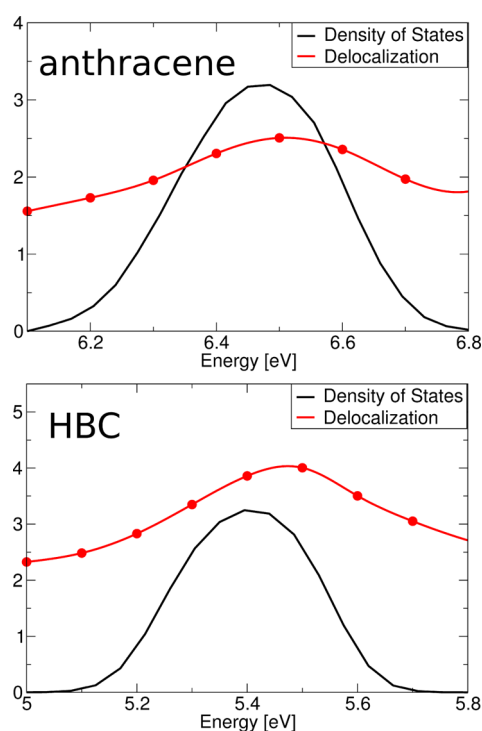


**Figure 7.** Density of states and number of molecules over which these states are delocalized averaged over all simulations of the anthracene *b*-direction.

these quantities are meant to facilitate the understanding of our charge-dynamics simulations.

For the ideal crystal or stack (no static and dynamic disorder), a delocalization over the entire system would occur, whereas dynamic disorder leads to localization of the states to 2–4 sites for the systems at finite temperatures. Because the adiabatic states, especially those at the tail of the DOS, are quite localized compared to the wave function that is observed in our Ehrenfest simulations, we can already conclude that the transport is nonadiabatic and occurs via occupation of higher adiabatic states. This is further quantified in Figure 8, where we show the percentage of adiabatic states that are occupied on average during our simulations. The occupation  $P_i = |b_i|^2$  of an adiabatic surface is obtained by projecting the wave function on the adiabatic states

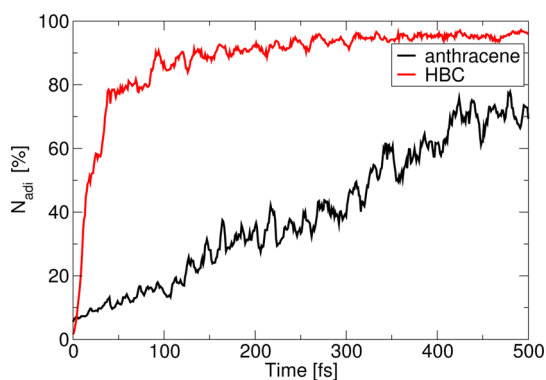


**Figure 8.** Percentage of adiabatic states that are occupied, averaged over 100 simulations. The simulation of the anthracene *b*-direction and HBC(1) are shown.

$$\Psi = \sum_m a_m |\phi_m\rangle = \sum_{im} |\phi_i\rangle \langle \phi_i | \phi_m \rangle a_m = \sum_i b_i |\phi_i\rangle \quad (24)$$

The ratio of occupied adiabatic states is defined as  $N_{\text{adi}} = \frac{1}{\sum_i p_i^2} \times \frac{1}{N_{\text{tot}}}$  where  $N_{\text{tot}}$  is the total number of adiabatic surfaces. Note that only the highest adiabatic states, resulting from linear combinations of the HOMOs, are present in our calculations. At the end of our simulations, approximately two-thirds of the adiabatic states are occupied in anthracene and nearly all states of HBC. Surprisingly, the occupation of additional adiabatic states sets in significantly more quickly in HBC compared to anthracene. This might in part be explained by the smaller nuclear relaxation of HBC (see Figure 5), which leads to a smaller stabilization of the adiabatic ground state at the starting conditions and facilitates the occupation of higher states. The faster transition from a single adiabatic state into an ensemble in HBC compared to anthracene gives rise to a stronger impact of the mean-field error, which also leads to an overestimation of the mobility in this case.

**3.7.1. Relevance of Lower-Lying Orbitals.** As mentioned above, the basis set of the FO Hamiltonian can be expanded if desired for a more accurate description of the system. For anthracene, this has only a negligible influence on the mobility because HOMO-1 lies  $\sim 1$  eV below the HOMO. Our calculations show an increase of mobility by  $\sim 10\%$ , which is within the error of our method. HBC, on the other hand, features a much more involved electronic structure. Besides the degenerate HOMO orbitals, there is also a relatively high-lying HOMO-2.

To evaluate the energy difference between HOMOs and HOMO-2, we applied the SAOP method<sup>70,71</sup> as a reference because it yields accurate orbital energies due to the correct asymptotic behavior of the exchange-correlation potential. The reference calculation on the structure optimized at the PW91/TZ2P level yields 0.271 eV for the energy difference, which is reasonably well reproduced by the DFTB1 value of 0.390 eV. Note that Hartree–Fock calculations, on the other hand, overestimate the energy difference of these orbitals tremendously with 0.685 eV. Further orbitals are well separated by more than 1 eV and are therefore omitted safely.

A further factor that increases the importance of HOMO-2 is the staggered stacking of molecules along the liquid crystalline columns, leading to minimal electronic coupling<sup>72</sup> between the degenerate HOMOs of neighboring molecules, whereas the coupling between HOMO-2 shows a maximum (see Figure 9).

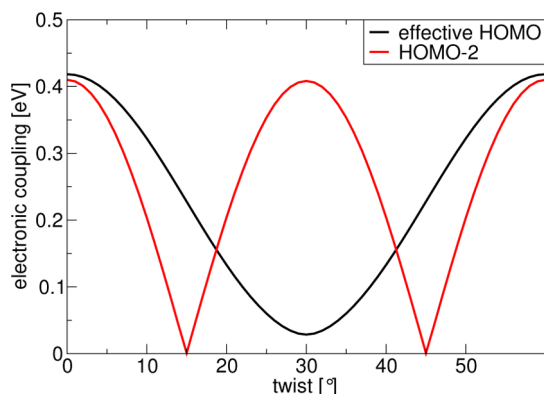


**Figure 9.** Dependence of the electronic couplings on the relative rotation of two HBC molecules around the columnar axis.

The cumulative effect of these large couplings leads to the surprising behavior that the HOMO of the stack is not a linear combination of the HOMOs of the individual molecules but rather of their HOMO-2, as can be seen in Figure 10.

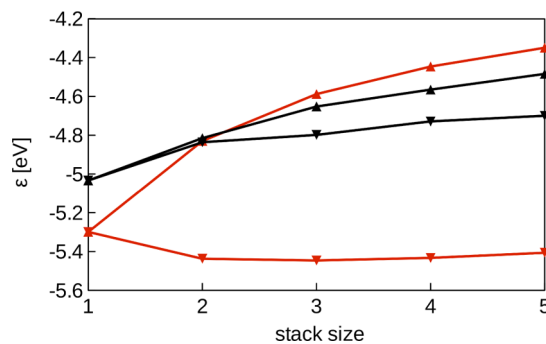


**Figure 10.** Energies of molecular orbitals for an HBC stack of different sizes calculated at the PBE/def2-TZVP level. Only the energetically highest (▲) and lowest (▼) linear combination of HOMOs (black) and HOMO-2 (red) of the single molecules are shown.

Therefore, HOMO-2 plays the dominant role in the propagation of the charge carrier, and its inclusion increases the mobility tremendously from 1.16 to 7.05  $\text{cm}^2 \text{V}^{-1} \text{s}^{-1}$ ), whereas inclusion of HOMO-3 has no further impact on the mobility (7.15  $\text{cm}^2 \text{V}^{-1} \text{s}^{-1}$ ). Note that the inclusion of the lower-lying HOMO-2 increases the deviation of the calculated mobility from the experimental value. However, experimental preparation conditions can have a much larger influence on the device performance and affect the mobility by several orders of magnitude.<sup>73,74</sup> Therefore, the importance of HOMO-2 cannot be discarded solely by comparison of the calculated mobility with the experiment. Furthermore, because our method overestimates the difference between the HOMOs and HOMO-2 compared to the reference calculation, we are confident that HOMO-2 actually plays an important role.

The dominant influence of lower-lying FOs is an uncommon mechanism and usually not considered when the optimization of mobilities is discussed. The prevalent guiding principle is still maximization of the intermolecular HOMO coupling as well as minimization of the energetic disorder and reorganization energy. Our calculations suggest that also the increase of the coupling between lower-lying FOs and the decrease of their stabilization with respect to the HOMO level should be considered as an additional route. Hopping calculations, as previously performed for HBC,<sup>12,13,75</sup> usually consider only the (degenerate) HOMOs or use constrained DFT to calculate electronic couplings. This way the influence of lower lying orbitals cannot be captured. Ehrenfest simulations in an AO basis, conversely, incorporate the influence of lower molecular orbitals only implicitly. Further analysis of the simulated charge dynamics is necessary to make the explicit connection between the transport through the bulk material, described in an AO basis, and the MO structure of the individual molecules. The FO method presented here is therefore a valuable tool for guiding the design of new molecular semiconductors by drawing a connection between the electronic structure of the synthesized monomer and its performance in the bulk material.

## 4. DISCUSSION AND CONCLUSIONS

We have developed a multiscale methodology that is capable of a quantitative description of the charge transport dynamics in

organic semiconductors, which can also unravel the mechanistic details of transport. The method includes local and nonlocal electron–phonon couplings explicitly via coupled equations of motions for the charge carrier and the nuclear degrees of freedom. An essential feature of our method is the combination of a linear-scaling fragment orbital approach with classical molecular dynamics, which allows access to extensive length and time scales that are necessary for a realistic description of bulk materials. Furthermore, corrections to the SI error of DFT are introduced. The charge transfer parameters have been shown to be very accurate, which allows a detailed description of the relevant processes.

As a result, our method can reproduce the absolute value as well as anisotropy of hole mobility in anthracene and HBC. Besides reproduction of experimental measurements, a detailed understanding of the charge transport mechanism is also accessible. The adiabatic eigenstates of the system are localized on a few molecules due to thermal disorder at all times. We consider the estimates of the localization to be reliable because their DFT delocalization error was corrected. Furthermore, we have observed that it is insufficient to consider only the two degenerate HOMOs of HBC in the hole dynamics, as often assumed in hopping models, because lower lying orbitals can have a significant influence on the mobility. No stable polaron was found for both materials at the simulated temperature, a finding similar to recent reports for other systems.<sup>7,76</sup> The “nonexistence” of the small polaron for materials with high mobility has been discussed in detail in ref 22; therefore, the success of hopping models for such materials<sup>12,13,75,77</sup> seems to be based on fortunate cancellation of errors.

We expect that such a bottom-up approach can complement experimental efforts in the understanding of the complex interplay between molecular structure and charge transport characteristics, and that it will become a valuable tool in the rational design of OSC with improved charge transport properties. The method shows its strengths for materials where a crossover of mechanisms is expected because it does not rely on a specific mechanism. For the description of totally disordered amorphous materials, hopping models are definitely better suited, in particular because simulation time scales have to be very long due to their very low mobilities and the localized character of the charge carrier. Pure crystals, conversely, can be treated with model approaches parametrized from DFT in most cases due to their high periodic order. Therefore, they are also not the main application area of this multiscale approach. Definitely interesting are materials with morphologies that are between totally ordered and disordered, where the excess charge gets partially localized by fluctuations, which may require a dynamic approach.

Despite its strengths, the proposed approach also has several shortcomings, which have been characterized well:

#### (1). Quantum Back Reaction and Mean Field Error.

The presence of excess charge introduces a distortion in the nuclear system (quantum back reaction), which in turn changes the electronic dynamics. In the Ehrenfest description, the charge is not restricted to a single adiabatic surface because the propagation of the time-dependent Schrödinger equation allows for the occupation of an ensemble of adiabatic states. In this way, the potential energy of the system is also, however, an average over all (adiabatic) states weighted by their occupation. The nuclear dynamics of the system then follows this mean potential energy surface (PES), whereas each member of the ensemble should in principle relax according

to its respective adiabatic PES leading to diverging trajectories. Therefore, relaxation of the molecular structure will be progressively underestimated with the increasing degree of delocalization. This drawback is significant, for example, whenever two adiabatic states with localized charge diverge in a polar environment, which has been discussed in detail for CT in DNA.<sup>32</sup> The different PESs, arising from each adiabatic state, will differ significantly and propagating the atoms on an averaged PES will therefore lead to qualitatively wrong dynamics. In the studied OCS, on the other hand, the adiabatic states are spread out over several sites, and the local relaxation (reorganization energy  $\lambda_i$ ) is very small. The relaxation of site  $m$  can be written as a function of charge<sup>32</sup> as  $E_{\text{rel}}^m = \frac{1}{2}\lambda_i Q_m^2$ , i.e., it becomes negligible (assuming the reorganization energies  $\lambda_i \approx 0.1$  eV) for a delocalization over 4 sites when compared to the thermal site energy fluctuations. Therefore, the Ehrenfest mean-field error probably does not contribute much to the error in the mobilities.

**(2). Non-Boltzmann Population in Ehrenfest Simulations.** On one hand, we have the problem that an entire ensemble is described with a single Ehrenfest trajectory. On the other hand, the ensemble does not obey a Boltzmann population.

We have seen that the adiabatic state populations, reached during our Ehrenfest simulations, do not obey a Boltzmann distribution. Note that this behavior is an intrinsic problem of the Ehrenfest method and does not result from the approximations of our methodology. Similar spreading over all adiabatic states was also found in ab initio Ehrenfest dynamics.<sup>53</sup> By restricting the transitions from lower to higher surfaces with a Boltzmann factor, however, the authors were able to suppress this behavior and achieve dynamics similar to a surface hopping simulation.

One could ask whether the artificial population of thermally nonaccessible states may affect the mobilities. In the case of anthracene, all adiabatic states are built from the same fragment orbital due to the large energetic separation of the HOMO from the remaining molecular orbitals. Therefore, we find similar electronic couplings between the sites no matter which adiabatic state is occupied, and thus do not expect the CT characteristic to be affected here. In the case of HBC, on the other hand, adiabatic states can be built from either degenerate HOMOs or HOMO-2, whereby the electronic couplings between the latter ones are significantly higher than between the former ones. Therefore, one can expect that allowing the occupation of thermally forbidden states affects the CT depending on the contribution of HOMOs and HOMO-2 to the respective state.

**(3). Electronic Polarization.** In our method, only the polarization of the neutral sites by the point charges of the environment are considered. However, a charged site would also polarize its environment, which in turn would cause additional energy shift. As long as all sites have (nearly) the same environment, like in the crystal and liquid crystal studied here, the stabilization is only a constant value, which can therefore be omitted. In amorphous materials, on the other hand, the sites have environments with different polarizabilities and their site energies will therefore shift differently.

One option to capture the influence of electronic polarization on the site energies is to perform constraint DFT (CDFT) calculations of the complex, where the charge is constrained to the respective molecule.<sup>78</sup> However, describing the whole



complex with CDFT is too expensive for the studied systems; furthermore, CDFT calculations are computationally less stable than FO calculations and therefore difficult to apply along MD simulations in a black-box manner. Besides that, the constraint will always place the excess charge in the HOMO/LUMO of the respective molecule, whereas in cases of (nearly) degenerate orbitals, there are several states close in energy that are equally important for the transport.

A better suited method is the recently proposed quantum patch approach,<sup>11,79</sup> where electronic polarization is described by charging one molecule and then self-consistency is obtained by relaxing the density of every molecule in the electric field of its neighbors. Because the molecular densities are relaxed stepwise in individual molecular calculations, linear scaling is achieved.

To summarize, for the two materials with sizable mobilities, no polaronic effects were found, and the charge carriers are substantially delocalized. This, however, implies that the quantum back reaction is not a critical issue, and it has been neglected from the beginning, as seen in ref 53. We have argued that Ehrenfest dynamics, which have several flaws that should be considered seriously, are applicable in this context. Because polaronic effects are small, the factors governing CT in these materials are the values and the fluctuations of the CT parameters, i.e., the site energies  $\epsilon_m$  and the couplings  $H_{mn}$ . As has been shown before,<sup>21</sup> the average couplings for a certain material can be very small, but the fluctuations can be such that transfer is governed by nonequilibrium structures. This highlights the importance of bottom-up modeling. The variations of  $H_{mn}$  are quite complex and not easy to implement into simple models. Therefore, atomistic simulations may be indispensable to understand material characteristics.

## 5. APPENDIX

### 5.1. Self-Interaction Error

It is well known that the total energy of an isolated molecule with fractional charge has to follow a straight line connecting the states with  $N$  and  $N - 1$  electrons.<sup>80</sup> The slope of the energy can be identified with the ionization potential or HOMO energy.<sup>81</sup> However, this is only true if an exact Hamiltonian is applied. DFT as well as HF energies deviate from the straight line for fractional occupations of a molecule. Furthermore, their HOMO energies are spuriously dependent on the fractional charge. Here, we will show the effect of the SI error on the charge carrier dynamics on the basis of a simple model.

Our model system consists of two sites  $A$  and  $B$  without any electron-phonon coupling. First, we use a charge-independent Hamiltonian for the simulation without any SI error:

$$H = H_0 = \begin{pmatrix} \epsilon_A & J \\ J & \epsilon_B \end{pmatrix} \quad (25)$$

with the site energies  $\epsilon_A = \epsilon_B = 0$ , and the electronic coupling  $J = 50$  meV, which is a reasonable value for  $\pi$ -stacked molecules. Propagation of an initially localized wave function with this Hamiltonian leads to the expected time evolution, as shown at the top of Figure 11. Because we do not start in an eigenstate of  $H_0$ , an oscillation with a frequency of 40 fs can be observed, and the wavefunction gets completely transferred between site  $A$  and  $B$ .

In previous applications on biomolecules,<sup>30,32</sup> a QM energy term was used with additional charge dependent contributions

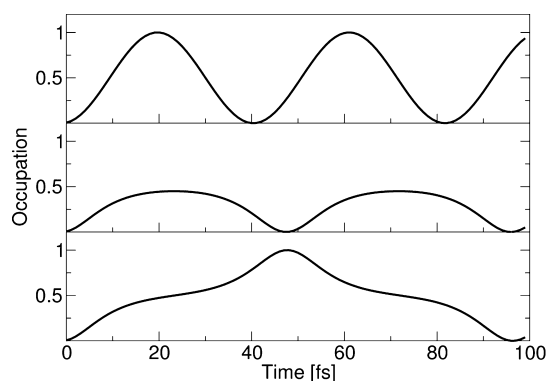


**Figure 11.** Time evolution of acceptor occupation in a two site system (top) without artificial stabilization of the delocalized state ( $E_{\text{del}} = 0$ ,  $J = 50$  meV) and with delocalization with energy smaller (mid) or larger (bottom) than the coupling ( $J = 50$  meV,  $E_{\text{del}} = J \pm 1$  meV). Artificial stabilization hinders the transfer and can even prevent complete transfer.

$$E_{\text{QM}}^+ = - \sum_{AB} c_A^* c_B H_{AB}^0 + \frac{1}{2} \sum_{AB} |c_A|^2 |c_B|^2 \gamma_{AB} \quad (26)$$

leading to a charge-dependent Hamiltonian

$$H_{AB} = -H_{AB}^0 + \delta_{AB} \sum_K (\gamma_{AK}) \Delta q_K \quad (27)$$

where,  $\gamma_{AA}$  is a molecular Hubbard parameter, describing charge dependent relaxation effects,  $\gamma_{AB}$  describes electrostatic interactions between the charged sites with  $1/R_{AB}$ , and  $\Delta q_K$  is the occupation of site  $K$ . As parameters, we take the same  $H_0$  as in eq 25, set  $\gamma_{AB} = 4.0$  eV, representing the electrostatic repulsion of partial charges in 3.5 Å distance, and take a molecular Hubbard parameter of  $\gamma_{AA} = 5.4$  eV, which is a reasonable value for medium-sized  $\pi$ -systems. When this Hamiltonian is used for the propagation, the charge transfer is completely prohibited, and the initial wave function stays localized at its initial site. It was pointed out that the introduction of charge-dependent terms to achieve a self-consistent Hamiltonian has effects similar to the SI in DFT, leading to over-delocalization and erroneous dissociation behavior.<sup>55</sup> Therefore, this example to some extent also shows the problems one might encounter with SI-prone methods in general. It was proposed to scale the second terms in eq 27 with a factor of 0.2 to mitigate the SI of the additional charge carrier.<sup>32</sup> However, even with the scaled second order terms, only a small fraction of charge gets transferred to the acceptor.

Following the work of Irle et. al., we will quantify the artificial stabilization.<sup>55</sup> Minor differences are that in our QM/MM framework the QM energy of the cationic system is calculated relative to the neutral MM reference system, and we are ignoring spin polarization. The general findings are the same however. Like above, we consider a symmetric dimer and calculate the site energy of a monomer in different charge states.

$$E(A) = 0 \quad (28)$$

$$E(A^+) = -\epsilon_A + \frac{1}{2} \gamma_{AA} \quad (29)$$

$$E(A^{+0.5}) = -\frac{1}{2}\epsilon + \frac{1}{2} \times 0.5 \times 0.5 \times \gamma_{AA} = -\frac{1}{2}\epsilon + \frac{1}{8}\gamma_{AA} \quad (30)$$

where  $E(A)$ ,  $E(A^+)$ , and  $E(A^{+0.5})$  are the energies of the molecule with a net charge of zero, one, and one half, respectively. The delocalization energy, that is, the stabilization of the delocalized solution compared to the localized one, is at infinite distances

$$E_{\text{del}}(R = \infty) = 2E(A^{+0.5}) - E(A) - E(A^+) = -\frac{1}{4}\gamma_{AA} \quad (31)$$

Although the delocalization error is largest at infinite distance, spurious stabilization of the delocalized solution can be expected at all distances. At smaller distances, however, additional contributions to the delocalization energy emerge. For fragments at vdW distance and beyond, the orbital overlap is small, and therefore, the interaction between the two fragments is dominated by coulomb interactions. This causes an additional charge repulsion term for the delocalized solution

$$E_{\text{coul}} = 0.5 \times 0.5 \times \gamma_{AB}(R_{AB}) \quad (32)$$

which is positive for all separation distances  $R_{AB}$  of the monomers and therefore counteracts the delocalization. The delocalization energy due to the self-interacting charge is therefore

$$\begin{aligned} E_{\text{del}}(R_{AB}) &= 2E(A^{+0.5}) - E(A) - E(A^+) + E_{\text{coul}} \\ &= -\frac{1}{4}(\gamma_{AA} - \gamma_{AB}) \end{aligned} \quad (33)$$

After quantifying the artificial stabilization, we wanted to see what happens for  $|J| > |E_{\text{del}}|$  and  $|J| < |E_{\text{del}}|$ . As long as the delocalization energy is larger than the coupling, the charge never gets completely transferred to the acceptor, as can be seen in the middle panel of Figure 11. For the case where the coupling is larger than the delocalization energy, there is an oscillation between sites A and B; however, the transfer is significantly hindered compared to the previous SI-free propagation. The influence of the relation of  $J$  and  $E_{\text{del}}$  further confirms the delocalization energy as cause of the unphysical dynamics.

Note that the fluctuation of site energies, caused by electron-phonon coupling, will obscure the erroneous dynamics. In aqueous environments,<sup>30,32–34</sup> the polarization of the environment leads to site energy differences of more than 1 eV, which completely overrules the effect of the SI error. In organic semiconductors, however, the site energy differences are significantly smaller. Therefore, simulations of anthracene with the charge-dependent Hamiltonian lead to the described trapping of the charge carrier on one site.

Surprisingly, similar simulations of the organic semiconductor coronene with a similar methodology showed no self-trapping.<sup>28</sup> In this study, an FO Hamiltonian was constructed from independent DFT calculations of the partially occupied sites in the electric field of their partially occupied neighbors. Therefore, these calculations should in principle also suffer from an SI error. However, as we just showed, the SI error manifests if  $J < E_{\text{del}}$ , and in coronene, the coupling is larger than in anthracene.<sup>5,13</sup> Additionally, the coronene starting structure in this study was a quite disordered stack with no ordered column and deviation from the ordered columnar structure can further enhance the electronic coupling

significantly.<sup>13</sup> Furthermore, the SI error is larger for high intermolecular distances,<sup>36</sup> which would further explain why trapping is observed in the relatively distant molecules in the herringbone anthracene crystal but not in the  $\pi$ -stacked coronene columns.

## 5.2. Lagrangian Equations

The Lagrangian in FO basis reads

$$\begin{aligned} L &= \sum_K \frac{1}{2} M_K \dot{R}_K^2 - i \sum_{mn} [a_m^* a_n \langle \phi_m | \dot{\phi}_n \rangle + a_m^* \dot{a}_n \langle \phi_m | \phi_n \rangle] \\ &\quad - E_{\text{MM}}^{\text{tot}} + \sum_{mn} a_m^* a_n \langle \phi_m | H[\rho_0] | \phi_n \rangle - \sum_m |a_m|^2 \frac{\Delta q_{\alpha}^m q_K^0}{R_{\alpha K}} \end{aligned} \quad (34)$$

Using the Lagrangian equation for the electronic degrees of freedom

$$\frac{\partial L}{\partial a_m^*} - \frac{d}{dt} \frac{\partial L}{\partial \dot{a}_m^*} = 0 \quad (35)$$

where

$$\frac{\partial L}{\partial \dot{a}_m^*} = 0 \quad (36)$$

we arrive at

$$\begin{aligned} \frac{\partial L}{\partial a_m^*} &= -i \sum_n [a_n \langle \phi_m | \dot{\phi}_n \rangle + \dot{a}_n \langle \phi_m | \phi_n \rangle] \\ &\quad + \sum_n a_n \left[ \langle \phi_m | H[\rho_0] | \phi_n \rangle - \delta_{mn} \sum_{\alpha} \sum_K \frac{\Delta q_{\alpha}^m q_K^0}{R_{\alpha K}} \right] \end{aligned} \quad (37)$$

Because we are using an orthogonal basis  $\langle \phi_m | \phi_n \rangle = \delta_{mn}$ , we arrive at

$$\dot{a}_m = -i \sum_n H_{mn} a_n - \sum_n a_n \langle \phi_m | \dot{\phi}_n \rangle \quad (38)$$

where  $H_{mn}$  is the FO Hamilton matrix including QM/MM interaction terms as defined in eq 19.

The Lagrange equation for the nuclear degrees of freedom is given by

$$\frac{d}{dt} \frac{\partial L}{\partial \dot{R}_k} = \frac{\partial L}{\partial R_k} \quad (39)$$

which yields

$$M_K \ddot{R}_k = -\frac{\partial E_{\text{MM}}^{\text{tot}}}{\partial R_k} + \sum_{mn} a_m^* a_n \frac{\partial}{\partial R_k} \langle \phi_m | H[\rho_0] | \phi_n \rangle - \frac{\partial}{\partial R_k} \Delta E^{\text{QM/MM}} \quad (40)$$

By expanding the FOs in AOs

$$|\phi_m\rangle = \sum_{\mu} c_{\mu}^m |\mu\rangle \quad (41)$$

we obtain within the applied DFTB1 Hamiltonian for the second term on the right-hand side of eq 40

$$\left( \sum_{mn} a_m^* a_n \frac{\partial}{\partial R_k} \langle \phi_m | H[\rho_0] | \phi_n \rangle \right) = \sum_{mn} \sum_{\mu\nu} a_m^* a_n c_{\mu}^m c_{\nu}^n \frac{\partial H_{\mu\nu}^0}{\partial R_k} \quad (42)$$

with  $\frac{\partial H_{\mu\nu}^0}{\partial R} = \langle \frac{\partial \mu}{\partial R} | H | \nu \rangle + \langle \mu | \frac{\partial H}{\partial R} | \nu \rangle + \langle \mu | H | \frac{\partial \nu}{\partial R} \rangle$  being the derivative of the tabulated DFTB1 matrix elements.

However, the FOs are not only *explicitly* dependent on  $R$  via  $|\mu\rangle$ . The displacement of an atom is also accompanied by a change of the expansion coefficients  $c_\mu^m$  in order to restore the norm of the FO  $m$ . For the correct forces to be obtained, it is therefore necessary to get the change of the total energy with respect to all quantities depending explicitly and implicitly on the atomic coordinates.<sup>82,83</sup> The change in overlap between two AOs is largest for neighboring atoms in the same fragment, whereas atoms located on different fragments have significantly smaller overlap due to its exponential decay. Following this reasoning, the implicit dependence on  $R$  is only considered in the diagonal elements of the coarse-grained Hamiltonian.

$$\begin{aligned} \frac{\partial}{\partial R_k} \langle \phi_m | H[\rho_0] | \phi_m \rangle &= \sum_{\mu\nu} c_\mu^m c_\nu^m \frac{\partial H_{\mu\nu}^0}{\partial R_k} \\ &+ \sum_{\mu\nu} \left( \frac{\partial c_\mu^m}{\partial R_k} H_{\mu\nu}^0 c_\nu^m + c_\mu^m H_{\mu\nu}^0 \frac{\partial c_\nu^m}{\partial R_k} \right) \end{aligned} \quad (43)$$

Here, the first term is the derivative of quantities explicitly dependent on  $R$ , which was already present in eq 42, whereas the second term captures the additional change of  $c_\mu^m$  that is necessary to conserve the norm. Because the FOs are (orthogonalized) eigenfunctions of the respective fragment, we approximate

$$\sum_{\mu} H_{\mu\nu}^0 c_\nu^m \approx \epsilon_m \sum_{\mu} S_{\mu\nu} c_\nu^m \quad (44)$$

which transforms the second sum of eq 43 into

$$\sum_{\mu\nu} \epsilon_m S_{\mu\nu} \frac{\partial (c_\mu^m c_\nu^m)}{\partial R_k} = \epsilon_m \frac{\partial}{\partial R_k} \left( \sum_{\mu\nu} S_{\mu\nu} c_\mu^m c_\nu^m \right) - \epsilon_m \sum_{\mu\nu} c_\mu^m c_\nu^m \frac{\partial S_{\mu\nu}}{\partial R_k} \quad (45)$$

Now, we can demand that the norm of the FO does not change

$$\frac{\partial}{\partial R_k} \langle \phi_m | \phi_m \rangle = \frac{\partial}{\partial R_k} \left( \sum_{\mu\nu} S_{\mu\nu} c_\mu^m c_\nu^m \right) = 0 \quad (46)$$

which eliminates the first term on the right-hand side of eq 45. With this, we get for the diagonal terms of eq 43

$$\frac{\partial}{\partial R_k} \langle \phi_m | H[\rho_0] | \phi_m \rangle = \sum_{\mu\nu} c_\mu^m c_\nu^m \left( \frac{\partial H_{\mu\nu}^0}{\partial R_k} - \epsilon_m \frac{\partial S_{\mu\nu}}{\partial R_k} \right) \quad (47)$$

Within the DFTB1 method, this is equivalent to  $\frac{\partial (E^0 - E^+)}{\partial R}$ , where  $E$  is the total energy of one fragment molecule in the neutral state and with the charge in orbital  $m$  within the frozen orbital approximation.

For a practical evaluation of the QM/MM coupling term of eq 17

$$\frac{\partial}{\partial R_k} \Delta E^{\text{QM/MM}} = \frac{\partial}{\partial R_k} \sum_{\alpha A} \frac{\Delta q_\alpha q_A^0}{|R_\alpha - R_A|} \quad (48)$$

the instantaneous Mulliken charges of the hole wave function  $\Delta q_\alpha$  are added to the force field, which then handles the calculation of forces. The total force expression for the complex is therefore

$$\begin{aligned} M_K \ddot{R}_k &= - \frac{\partial E_{\text{MM}}^{\text{tot}}(q_A^0, \Delta q_\alpha)}{\partial R_k} \\ &+ \sum_{mn} \sum_{\mu\nu} a_m^* a_n c_\mu^m c_\nu^n \left( \frac{\partial H_{\mu\nu}^0}{\partial R_k} - \delta_{mn} \epsilon_m \frac{\partial S_{\mu\nu}}{\partial R_k} \right) \end{aligned} \quad (49)$$

where  $E_{\text{MM}}^{\text{tot}}(q_A^0, \Delta q_\alpha)$  denotes the force field energy of the total system with adapted partial charges.

## AUTHOR INFORMATION

### Corresponding Author

\*E-mail: [marcus.elstner@kit.edu](mailto:marcus.elstner@kit.edu). Phone: +49 721 608-45705. Fax: +49 721 608-45710.

### Notes

The authors declare no competing financial interest.

## ACKNOWLEDGMENTS

A.H. was supported by graduate funding from the German states. The simulations were carried out on BwForCluster JUSTUS (Ulm) and InstitutsCluster II (Karlsruhe).

## REFERENCES

- (1) Dong, H.; Fu, X.; Liu, J.; Wang, Z.; Hu, W. *Adv. Mater.* **2013**, *25*, 6158–6183.
- (2) Brédas, J. L.; Calbert, J. P.; Filho, D. S.; Cornil, J. *Proc. Natl. Acad. Sci. U. S. A.* **2002**, *99*, 5804–5809.
- (3) Coropceanu, V.; Cornil, J.; da Silva Filho, D. A.; Olivier, Y.; Silbey, R.; Brédas, J.-L. *Chem. Rev.* **2007**, *107*, 926–952.
- (4) Troisi, A.; Orlandi, G. *Phys. Rev. Lett.* **2006**, *96*, 086601.
- (5) Troisi, A.; Orlandi, G. *J. Phys. Chem. A* **2006**, *110*, 4065–4070.
- (6) Troisi, A. *Adv. Mater.* **2007**, *19*, 2000–2004.
- (7) Troisi, A. *Chem. Soc. Rev.* **2011**, *40*, 2347–2358.
- (8) Gershenson, M. E.; Podzorov, V.; Morpurgo, A. F. *Rev. Mod. Phys.* **2006**, *78*, 973–989.
- (9) Nelson, J.; Kwiatkowski, J. J.; Kirkpatrick, J.; Frost, J. M. *Acc. Chem. Res.* **2009**, *42*, 1768–1778.
- (10) Kwiatkowski, J. J.; Nelson, J.; Li, H.; Brédas, J. L.; Wenzel, W.; Lennartz, C. *Phys. Chem. Chem. Phys.* **2008**, *10*, 1852–1858.
- (11) Friederich, P.; Symalla, F.; Meded, V.; Neumann, T.; Wenzel, W. *J. Chem. Theory Comput.* **2014**, *10*, 3720–3725.
- (12) Kirkpatrick, J.; Marcon, V.; Kremer, K.; Nelson, J.; Andrienko, D. *J. Chem. Phys.* **2008**, *129*, 094506.
- (13) Feng, X.; Marcon, V.; Pisula, W.; Hansen, M. R.; Kirkpatrick, J.; Grozema, F.; Andrienko, D.; Kremer, K.; Mullen, K. *Nat. Mater.* **2009**, *8*, 421–426.
- (14) Marcon, V.; Breiby, D. W.; Pisula, W.; Dahl, J.; Kirkpatrick, J.; Patwardhan, S.; Grozema, F.; Andrienko, D. *J. Am. Chem. Soc.* **2009**, *131*, 11426–11432.
- (15) Poelking, C.; Cho, E.; Malafeev, A.; Ivanov, V.; Kremer, K.; Risko, C.; Brédas, J.-L.; Andrienko, D. *J. Phys. Chem. C* **2013**, *117*, 1633–1640.
- (16) Rühle, V.; Kirkpatrick, J.; Andrienko, D. *J. Chem. Phys.* **2010**, *132*, 134103.
- (17) Vehoff, T.; Chung, Y. S.; Johnston, K.; Troisi, A.; Yoon, D. Y.; Andrienko, D. *J. Phys. Chem. C* **2010**, *114*, 10592–10597.
- (18) Vehoff, T.; Baumeier, B.; Troisi, A.; Andrienko, D. *J. Am. Chem. Soc.* **2010**, *132*, 11702–11708.
- (19) Vehoff, T.; Baumeier, B.; Andrienko, D. *J. Chem. Phys.* **2010**, *133*, 134901.
- (20) Ortmann, F.; Bechstedt, F.; Hannebald, K. *Phys. Status Solidi B* **2011**, *248*, 511–525.
- (21) McMahon, D. P.; Troisi, A. *ChemPhysChem* **2010**, *11*, 2067–2074.
- (22) Troisi, A. *Org. Electron.* **2011**, *12*, 1988–1991.
- (23) Gajdos, F.; Oberhofer, H.; Dupuis, M.; Blumberger, J. *J. Phys. Chem. Lett.* **2013**, *4*, 1012–1017.



- (24) Wang, L.; Beljonne, D. *J. Phys. Chem. Lett.* **2013**, *4*, 1888–1894.
- (25) Wang, L.; Beljonne, D. *J. Chem. Phys.* **2013**, *139*, 064316.
- (26) Kocherzhenko, A. A.; Grozema, F. C.; Siebbeles, L. D. A. *Phys. Chem. Chem. Phys.* **2011**, *13*, 2096–2110.
- (27) Stafstrom, S. *Chem. Soc. Rev.* **2010**, *39*, 2484–2499.
- (28) Gollub, C.; Avdoshenko, S.; Gutierrez, R.; Berlin, Y.; Cuniberti, G. *Isr. J. Chem.* **2012**, *52*, 452–460.
- (29) Gao, X.; Geng, H.; Peng, Q.; Ren, J.; Yi, Y.; Wang, D.; Shuai, Z. *J. Phys. Chem. C* **2014**, *118*, 6631–6640.
- (30) Kubař, T.; Elstner, M. *Phys. Chem. Chem. Phys.* **2013**, *15*, 5794–5813.
- (31) Kubar, T.; Elstner, M. *J. R. Soc., Interface* **2013**, *10*, 20130415.
- (32) Kubař, T.; Elstner, M. *J. Phys. Chem. B* **2010**, *114*, 11221–11240.
- (33) Lüdemann, G.; Solov'yov, I. A.; Kubař, T.; Elstner, M. *J. Am. Chem. Soc.* **2015**, *137*, 1147–1156.
- (34) Lüdemann, G.; Woiczikowski, P. B.; Kubař, T.; Elstner, M.; Steinbrecher, T. B. *J. Phys. Chem. B* **2013**, *117*, 10769–10778.
- (35) Woiczikowski, P. B.; Steinbrecher, T.; Kubař, T.; Elstner, M. *J. Phys. Chem. B* **2011**, *115*, 9846–9863.
- (36) Lundberg, M.; Siegbahn, P. E. M. *J. Chem. Phys.* **2005**, *122*, 224103.
- (37) Löwdin, P. O. *J. Chem. Phys.* **1950**, *18*, 365–375.
- (38) Kubas, A.; Hoffmann, F.; Heck, A.; Oberhofer, H.; Elstner, M.; Blumberger, J. *J. Chem. Phys.* **2014**, *140*, 104105.
- (39) Kubas, A.; Gajdos, F.; Heck, A.; Oberhofer, H.; Elstner, M.; Blumberger, J. *Phys. Chem. Chem. Phys.* **2015**, *17*, 14342–14354.
- (40) Kubař, T.; Woiczikowski, P. B.; Cuniberti, G.; Elstner, M. *J. Phys. Chem. B* **2008**, *112*, 7937–7947.
- (41) Voityuk, A. A. *Chem. Phys. Lett.* **2006**, *427*, 177–180.
- (42) Gaus, M.; Cui, Q.; Elstner, M. *WIREs Comput. Mol. Sci.* **2014**, *4*, 49–61.
- (43) Elstner, M.; Seifert, G. *Philos. Trans. R. Soc., A* **2014**, *372*, 20120483.
- (44) Porezag, D.; Frauenheim, T.; Köhler, T.; Seifert, G.; Kaschner, R. *Phys. Rev. B: Condens. Matter Mater. Phys.* **1995**, *51*, 12947–12957.
- (45) Seifert, G.; Porezag, D.; Frauenheim, T. *Int. J. Quantum Chem.* **1996**, *58*, 185–192.
- (46) Elstner, M.; Porezag, D.; Jungnickel, G.; Elsner, J.; Haugk, M.; Frauenheim, T.; Suhai, S.; Seifert, G. *Phys. Rev. B: Condens. Matter Mater. Phys.* **1998**, *58*, 7260–7268.
- (47) Gaus, M.; Cui, Q.; Elstner, M. *J. Chem. Theory Comput.* **2011**, *7*, 931–948.
- (48) Elstner, M. *J. Phys. Chem. A* **2007**, *111*, S614–S621.
- (49) Deumens, E.; Diz, A.; Longo, R.; Öhrn, Y. *Rev. Mod. Phys.* **1994**, *66*, 917–983.
- (50) In a simulation of an HBC dimer, the largest difference in these matrix elements was just  $7.3 \times 10^{-3}$ , and the RMSD was just  $1.2 \times 10^{-5}$  over the course of 100 fs.
- (51) van Aggelen, H.; Yang, Y.; Yang, W. *Phys. Rev. A: At., Mol., Opt. Phys.* **2013**, *88*, 030501.
- (52) Cohen, A. J.; Mori-Sánchez, P.; Yang, W. *Science* **2008**, *321*, 792–794.
- (53) Ren, J.; Vukmirović, N.; Wang, L.-W. *Phys. Rev. B: Condens. Matter Mater. Phys.* **2013**, *87*, 205117.
- (54) Körzdörfer, T.; Brédas, J.-L. *Acc. Chem. Res.* **2014**, *47*, 3284–3291.
- (55) Lundberg, M.; Nishimoto, Y.; Irle, S. *Int. J. Quantum Chem.* **2012**, *112*, 1701–1711.
- (56) Heck, A.; Woiczikowski, P. B.; Kubař, T.; Welke, K.; Niehaus, T.; Giese, B.; Skourtis, S.; Elstner, M.; Steinbrecher, T. B. *J. Phys. Chem. B* **2014**, *118*, 4261–4272.
- (57) Sutton, C.; Sears, J. S.; Coropceanu, V.; Brédas, J.-L. *J. Phys. Chem. Lett.* **2013**, *4*, 919–924.
- (58) Karl, N.; Marktanner, J. *Mol. Cryst. Liq. Cryst. Sci. Technol., Sect. A* **2001**, *355*, 149–173.
- (59) Fechtenkötter, A.; Tchegobotareva, N.; Watson, M.; Müllen, K. *Tetrahedron* **2001**, *57*, 3769–3783.
- (60) Brock, C. P.; Dunitz, J. D. *Acta Crystallogr., Sect. B: Struct. Sci.* **1990**, *46*, 795–806.
- (61) Wang, J.; Wolf, R. M.; Caldwell, J. W.; Kollman, P. A.; Case, D. A. *J. Comput. Chem.* **2004**, *25*, 1157–1174.
- (62) Bayly, C. I.; Cieplak, P.; Cornell, W.; Kollman, P. A. *J. Phys. Chem.* **1993**, *97*, 10269–10280.
- (63) Kalinowski, J. A.; Lesyng, B.; Thompson, J. D.; Cramer, C. J.; Truhlar, D. G. *J. Phys. Chem. A* **2004**, *108*, 2545–2549.
- (64) Páll, S.; Abraham, M.; Kutzner, C.; Hess, B.; Lindahl, E. In *Solving Software Challenges for Exascale*; Markidis, S., Laure, E., Eds.; Lecture Notes in Computer Science; Springer International Publishing, 2015; Vol. 8759, pp 3–27.
- (65) Aradi, B.; Hourahine, B.; Frauenheim, T. *J. Phys. Chem. A* **2007**, *111*, S678–S684.
- (66) te Velde, G.; Bickelhaupt, F. M.; Baerends, E. J.; Fonseca Guerra, C.; van Gisbergen, S. J. A.; Snijders, J. G.; Ziegler, T. *J. Comput. Chem.* **2001**, *22*, 931–967.
- (67) Ahlrichs, R.; Bär, M.; Häser, M.; Horn, H.; Kölmel, C. *Chem. Phys. Lett.* **1989**, *162*, 165–169.
- (68) Lemaire, V.; da Silva Filho, D. A.; Coropceanu, V.; Lehmann, M.; Geerts, Y.; Piris, J.; Debie, M. G.; van de Craats, A. M.; Senthikumar, K.; Siebbeles, L. D. A.; Warman, J. M.; Brédas, J.-L.; Cornil, J. *J. Am. Chem. Soc.* **2004**, *126*, 3271–3279.
- (69) van de Craats, A. M.; Warman, J. M.; Fechtenkötter, A.; Brand, J. D.; Harbison, M. A.; Müllen, K. *Adv. Mater.* **1999**, *11*, 1469–1472.
- (70) Gritsenko, O. V.; Schipper, P. R. T.; Baerends, E. J. *Chem. Phys. Lett.* **1999**, *302*, 199–207.
- (71) Schipper, P. R. T.; Gritsenko, O. V.; van Gisbergen, S. J. A.; Baerends, E. J. *J. Chem. Phys.* **2000**, *112*, 1344–1352.
- (72) Note that there are four different coupling elements between degenerate orbitals on two molecules and an effective coupling can be derived as  $H_{AB}^{\text{eff}} = \sqrt{\frac{1}{2} \sum_{m \in A, n \in B} |H_{mn}|^2}$ .
- (73) Tada, H.; Touda, H.; Takada, M.; Matsushige, K. *Appl. Phys. Lett.* **2000**, *76*, 873–875.
- (74) Li, L.; Tang, Q.; Li, H.; Yang, X.; Hu, W.; Song, Y.; Shuai, Z.; Xu, W.; Liu, Y.; Zhu, D. *Adv. Mater.* **2007**, *19*, 2613–2617.
- (75) Kirkpatrick, J.; Marcon, V.; Nelson, J.; Kremer, K.; Andrienko, D. *Phys. Rev. Lett.* **2007**, *98*, 227402.
- (76) Mozafari, E.; Stafström, S. *J. Chem. Phys.* **2013**, *138*, 184104.
- (77) Wade, J.; Steiner, F.; Niedzialek, D.; James, D. T.; Jung, Y.; Yun, D.-J.; Bradley, D. D. C.; Nelson, J.; Kim, J.-S. *J. Mater. Chem. C* **2014**, *2*, 10110–10115.
- (78) Ratcliff, L. E.; Grisanti, L.; Genovese, L.; Deutsch, T.; Neumann, T.; Danilov, D.; Wenzel, W.; Beljonne, D.; Cornil, J. *J. Chem. Theory Comput.* **2015**, *11*, 2077–2086.
- (79) Friederich, P.; Meded, V.; Symalla, F.; Elstner, M.; Wenzel, W. *J. Chem. Theory Comput.* **2015**, *11*, S60–S67.
- (80) Perdew, J. P.; Parr, R. G.; Levy, M.; Balduz, J. L. *Phys. Rev. Lett.* **1982**, *49*, 1691–1694.
- (81) Janak, J. F. *Phys. Rev. B: Condens. Matter Mater. Phys.* **1978**, *18*, 7165–7168.
- (82) Marx, D.; Hutter, J. *Ab Initio Molecular Dynamics: Basic Theory and Advanced Methods*, 1st ed.; Cambridge University Press, 2009; pp 51–56.
- (83) Fähnle, M.; Elsässer, C.; Krimmel, H. *Phys. Status Solidi B* **1995**, *191*, 9–19.